Outlet temperatures of a slinky-type Horizontal Ground Heat Exchanger with the atmosphere-soil interaction

Fujiao Tang, Hossein Nowamooz

Outlet temperatures of a slinky-type Horizontal Ground Heat Exchanger with the atmosphere-soil interaction

Fujiao Tang* & Hossein Nowamooz

ICUBE, UMR 7357, CNRS, INSA de Strasbourg, 24 boulevard de la Victoire, 67084 Strasbourg

*Corresponding author

Email address:

fujiao.tang@insa-strasbourg.fr (Fujiao Tang)

Highlights

- A numerical framework considering the atmosphere-soil interaction was constructed.
- The performance of a slinky-type Horizontal Ground Heat Exchanger was evaluated.
- The land surface temperature and heat flux were affected during the heating period.
- Non-consideration of the atmosphere-soil interaction led to higher outlet temperatures.
- The overestimation of the outlet temperature decreased as the installation depth increased.

Abstract

Generally, a Horizontal Ground Heat Exchanger (HGHE) is installed in shallow depths, which can influence the land surface temperature during its operation period, especially when a high heat demand is required. Consequently, the existing methods of using time-varying land surface temperatures are not sufficient for the HGHE simulations. In this paper, a numerical framework considering the atmosphere-soil-HGHE interaction was proposed and validated. The outlet temperatures of a slinky-type HGHE installed in a multi-layered soil field were then investigated under the heating scenario by considering the local meteorological and geological conditions. The results showed that the operation of the HGHE affected obviously the land surface temperature and the ground heat flux. The increase of the installation depth from 0.5 to 2 m increased the outlet temperatures. However, this increase was insignificant when the installation depth increased from 0.5 to 1 m. It was further identified that the non-consideration of the atmosphere-soil interaction overestimated the annual fluid outlet temperature in the heating scenario, and this overestimation decreased from 47.99% to 17.16% as the installation depth increased from 0.5 to 2 m. In conclusion, it is necessary to consider the atmosphere-soil interaction to predict precisely the outlet temperatures of a shallow HGHE.

Keywords

Horizontal Ground Heat Exchanger; Numerical modeling; Outlet temperatures; Land surface energy/water balance; Installation depth.

Nomenclature

A	U-pipe cross-sectional area, m^2
a_l	surface albedo
c_c	cloud cover
C_p	specific heat capacity, $Jkg^{-1}K^{-1}$
C_v	volumetric heat capacity, $Jm^{-3}K^{-1}$
d	displacement height, m
D	elevation head, m
e_a	actual vapor pressure, kPa
e_s	saturation vapor pressure, kPa
E	actual evaporation on the soil surface, mms^{-1}
E_p	evaporation potential, $kgm^{-2}s^{-1}$ or mms^{-1}
d_h	inner diameter of the U-pipe, m
f_D	Darcy friction factor
G	total heat flux through land surface, Wm^{-2}
h_c	vegetation height, m
h_{int}	heat transfer coefficient, $Wm^{-2}K^{-1}$
H	sensible heat flux, Wm^{-2}
H_k	kinetic head, m
H_p	water potential or suction head, m
k	thermal conductivity, $Wm^{-1}K^{-1}$
k_r	relative hydraulic conductivity
K	hydraulic conductivity, ms^{-1}
l	pore connectivity parameter
L	latent heat of vaporization for water, Jkg^{-1}
LAI	leaf area index
n	independent parameter
P	rainfall rate, mms^{-1}
P_{at}	atmospheric pressure, Pa
Q_s	soil heat source, Wm^{-3}
Q_{wall}	heat from the surrounding, Wm^{-1}
r_1	stomatal resistance of a single leaf, sm^{-1}
r_a	aerodynamic resistance to heat transfer, sm^{-1}
r_c	crop canopy resistance, sm^{-1}
r_{mw}	molecular weight of water vapor to dry air
R_a	income longwave radiation, Wm^{-2}
R_n	net radiation, Wm^{-2}
R_s	shortwave radiation, Wm^{-2}
RH	air humidity, %
S_e	relative saturation of soil
S_r	saturation of soil
t	time, s
T	temperature, °C or K
T_{in}	inlet temperature, °C
T_{out}	outlet temperature, °C
T_s	land surface temperature, K
T_{sky}	sky temperature, K
u	velocity, ms^{-1}
u_{wind}	wind speed, ms^{-1}
W_i	infiltration, mms^{-1}
W_r	water run off, mms^{-1}
x_s	gravimetric sand content
Z	U-pipe inner perimeter, m
z_m	height for measuring meteorological conditions, m
z_{oh}	water vapor roughness length, m
z_{om}	momentum roughness length, m

Greek symbols

Δ	slope of the saturation vapor pressure curve, $kPaK^{-1}$
α	independent parameter, m^{-1}
γ	psychrometric constant, $kPaK^{-1}$
γ_d	soil dry unit weights, kNm^{-3}
γ_s	soil specific unit weights, kNm^{-3}
ε	soil surface emissivity
θ	volumetric water content
κ	von Karman constant
ρ	density, kgm^{-3}
σ	Stephan-Boltzman constant, $Wm^{-2}K^{-4}$
ψ	specific moisture capacity, m^{-1}

Subscripts

a	air
f	carrying fluid
$i\text{-}p$	inner pipe wall
r	residual
s	soil
sat	saturated
w	water

1 Introduction

Renewable energy is continuing to gain importance due to the fact that traditional energy sources are not unlimited in the long run, especially for an epoch with increasing energy demand. Moreover, environmental risks such as air pollution, regional acidification and climate change [1] emerge gradually by consuming fossil fuels. Sangi and Müller [2] report that the European Union has set the goal to reduce its CO_2 emission by 20% till 2020 compared to the year 2007 and renewable energy is crucial for this aim to be achieved.

Shallow geothermal energy is among the many sources of renewable energy, and it can be easily accessed all around the world. The shallow geothermal energy system has an approximate lifespan of 40-50 years and is regarded as a semi-permanent energy system [3]. Generally, open and closed heat exchangers are available for the exploitation of shallow geothermal energy [4], which are then served as low-potential sources of thermal energy for heat pumps [5]. Horizontal Ground Heat Exchanger (HGHE) is one of those closed loop heat exchangers. Compared to Vertical Ground Heat Exchanger (VGHE), it is more cost effective although it requires more installation space [6]. The costs can be further reduced by using a slinky-type HGHE [7], which enables HGHE to be an appealing technology for residential and small non-residential applications [8]. However, due to the shallow installation depth (conventionally between 1.0 and 2.0 m) [9,10], it is more sensitive to the meteorological condition than VGHE.

In HGHE engineering, it is necessary to estimate accurately the performance of a given HGHE in the design stage [11]. Numerical modeling is the most popular method since it is comprehensive and can reduce the initial capital investment. Till now, several numerical simulations have been conducted to investigate the performance of a HGHE at different conditions. By using CFD code Fluent, Congedo et al. [12] find that increasing the installation

depth of a HGHE from 1.5 to 2.5 m does not play an important role on the system performance. However, they conclude that the ground thermal conductivity is the most important parameter for the heat transfer performance of their system. By developing an in-house numerical simulation program, Gan [13] finds that the soil freezing can generally increase the heat extraction rate of a HGHE. He observes especially that when the soil freezing happens in the vicinity of the pipe, the heat extraction rate increases 1.7% for the carrying fluid temperature of -1 °C. By using a transient three-dimensional finite volume model in ANSYS Fluent, Al-Ameen et al. [8] find that adopting mill-scale copper slag instead of Leighton buzzard sand as a backfill material increases the HGHE performance. By using the finite volume method, Habibi and Hakkaki-Fard [10] conclude that the slinky-type HGHE performs 75% and 9% better than the linear and spiral HGHEs, respectively. By using Midas NFX numerical program, Kim et al. [11] find that the pipe diameter influences negligibly the heat exchange rate of the HGHE. By using COMSOL Multiphysics simulations for a spiral HGHE, Go et al. [14] conclude that the increase of the flow rate generally has a positive influence on the HGHE performance. However, the total efficiency will decrease in inverse proportion to the flow rate if the coil pitch becomes too narrow.

Despite the popularity of the numerical simulations in HGHE engineering, there are some points often neglected or simplified in many numerical investigations.

Due to the complex atmosphere-soil interaction, time-varying land surface temperatures are often considered in the numerical simulations. For example, the atmosphere temperature is conventionally applied as a surface boundary [8,10,14-21]. Wu et al. [22] have experimentally investigated a slinky-type HGHE in an 80 m long by 20 m wide paddock area at a depth of around 1.2 m below the ground surface at Talbot Cottage, Drayton St Leonard site, Oxfordshire, UK. They discover that the ground surface temperature is higher when no heat

exchanger is installed, proving that the operation of the HGHE has influenced the land surface temperature. This means that time-varying land surface temperatures (such as atmosphere temperatures) might not be sufficient to estimate the HGHE performance. This point is often absent in the numerical simulations.

By measuring the soil thermal conductivity at five sites in Midwestern USA at the depth of 1.2 m, Naylor et al. [23] find that the soil moisture fluctuations result in a very significant variation of the soil thermal conductivity. Gan [24] concludes in his numerical simulations that the maximum differences of heat transfer through a HGHE between the models with and without moisture transfer are 24%, 17% and 18% in clay sand, loamy sand and sandy soils, respectively. Therefore, the consideration of the hydrothermal transfer in shallow zones is necessary for the design of HGHE, often neglected in the numerical simulations.

A slinky-type HGHE has a good performance and it is popular in real practice [2,10,25]. Linear-type and spiral-type HGHEs are often studied in the numerical simulations as their geometries are easier to be constructed [15]. However, numerical studies on slinky-type HGHE are limited due to its complex geometry.

The main objective of this investigation is to construct a robust numerical simulation framework to evaluate the HGHE performance in field conditions by considering energy and water balance on the land surface. This investigation also aims to visualize how the HGHE influences the land surface temperature and the heat flux through the land surface, rarely studied so far. Moreover, the investigation has compared the numerical simulation results under two different surface boundary conditions (with/without considering atmosphere-soil interaction), which helps to identify the reliability of the traditional method by setting time-varying temperature as land surface boundary.

In this context, a validated finite element model established in COMSOL is used to estimate

the performance of a HGHE installed in a multi-layered soil field. The above-mentioned neglected points such as land surface energy/water balance, hydrothermal fluctuations and a slinky-type HGHE are addressed in this numerical framework.

2 Governing Equations

Fig. 1 shows a schematic diagram of the concerning phenomenon in HGHE engineering. The necessary governing equations considering the atmosphere-soil-HGHE interaction are constituted of 4 parts: a) the soil surface energy balance; b) the soil surface water balance; c) the hydrothermal transfer in subsurface soil and d) the heat transfer in pipe.

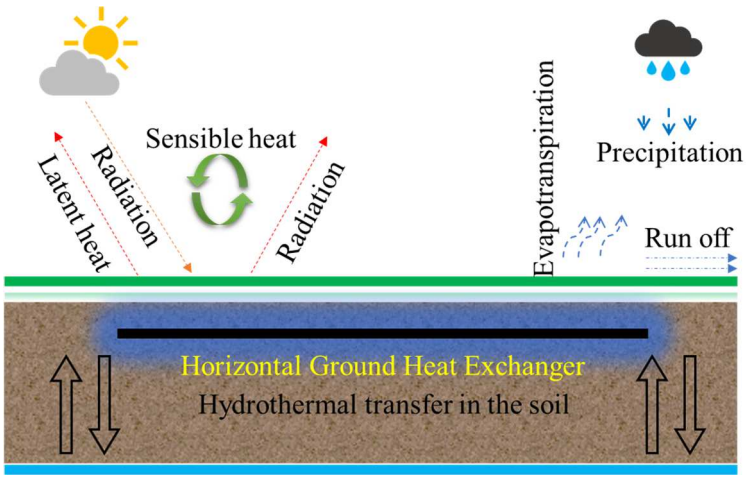

Fig. 1 Schematic diagram for the considered mechanism of the energy and water transfer in this study.

2.1 Soil surface energy balance

Energy balance on the land surface is given as [26]:

$$R_n + H - LE - G = 0 \tag{1}$$

where R_n is the net radiation heat flux (Wm^{-2}), H is the sensible heat flux (Wm^{-2}), LE is the latent heat flux (Wm^{-2}), G is the ground heat flux (Wm^{-2}). It should be noted that the net radiation and the sensitive heat flux have both positive and negative values while the latent

heat flux has only positive values. The ground heat flux indicates the total heat flux flow through the land surface. A positive value represents the heat flux into the ground. On the contrary, a negative value represents the heat flux out from the ground. To calculate the ground heat flux, it is necessary to obtain the net radiation heat flux, the sensitive heat flux and the latent heat flux.

At first, net radiation is the difference between the total incoming and outgoing radiations:

$$R_n = (1 - a_l)R_s + (R_a - \varepsilon\sigma T_s^{\,4}) \tag{2a}$$

where a_l is the surface albedo, R_s is the shortwave radiation (Wm^{-2}), R_a is the incoming longwave radiation (Wm^{-2}), $\varepsilon\delta T_s^4$ is the outcoming longwave radiation (Wm^{-2}), ε is the soil surface emissivity, σ is Stephan-Boltzman constant ($Wm^{-2}K^{-4}$), T_s is the soil temperature (K).

The net long wave radiation can be obtained by:

$$R_a - \varepsilon\sigma T_s^{\,4} = -\sigma\varepsilon(T_s^4 - T_{sky}^4) \tag{2b}$$

where sky temperature T_{sky} (K) is decided by cloud cover c_c and air temperature T_a (K) [27]:

$$T_{sky}^4 = 9.365574\times10^{-6}(1-c_c)T_a^6 + c_c[(1-0.84\cdot c_c)(0.527 + 0.161\cdot \mathrm{e}^{8.45(1-\frac{273.15}{T_a})}) + 0.84\cdot c_c]T_a^4 \tag{2c}$$

Secondly, it is the sensible heat flux, which is the convective heat transfer between the ground surface and the ambient air [28], given as:

$$H = \rho_a C_{p-a}(T_a - T_s)/r_a \tag{3a}$$

where ρ_a is the air density (kgm^{-3}), $C_{p\text{-}a}$ is the air specific heat capacity ($Jkg^{-1}K^{-1}$), r_a is the aerodynamic resistance to heat transfer (sm^{-1}).

The aerodynamic resistance is given as [29]:

$$r_a = \frac{\ln(\frac{z_m - d}{z_{om}}) \cdot \ln(\frac{z_m - d}{z_{oh}})}{\kappa^2 u_{wind}} \quad (3b)$$

where z_m is the height where the meteorological parameters are measured (m), d is the displacement height (m), z_{om} is the roughness length for momentum (m), z_{oh} is the roughness length for water vapor (m), κ is the von Karman constant, and u_{wind} is the wind speed (ms^{-1}).

The displacement height is linear to the vegetation height h_c (m):

$$d = 2h_c / 3 \quad (3c)$$

The roughness length for momentum transfer is calculated by:

$$z_{om} = 0.123 h_c \quad (3d)$$

The roughness length for vapor transfer is:

$$z_{oh} = 0.1 z_{om} \quad (3e)$$

Finally, the latent heat flux is represented by *LE*, constituted by the latent heat vaporization of water L (Jkg^{-1}) and the actual evaporation E (mms^{-1}). The actual evaporation can be obtained by the following equation [30-33]:

$$E = P \cdot \left[1 + (E_p / P)^{-2}\right]^{-\frac{1}{2}} \quad (4a)$$

where P is the rainfall rate (mms^{-1}), E_p is the evaporation potential ($kgm^{-2}s^{-1}$ or mms^{-1}).

The evaporation potential is obtained by Penman-Monteith formulation [34]:

$$E_p = \frac{1}{L}\left[\frac{\Delta \cdot R_n + \rho_a C_{p-a}(e_s - e_a) / r_a}{\Delta + \gamma(1 + r_c / r_a)}\right] \quad (4b)$$

where Δ is the slope of the saturation vapor pressure curve ($kPaK^{-1}$), e_s is the saturation vapor

pressure (kPa), e_a is the actual vapor pressure (kPa), γ is the psychrometric constant ($kPaK^{-1}$), r_c is the crop canopy resistance (sm^{-1}).

The slope of the saturation vapor pressure is given by:

$$\Delta = 4098 e_s / (T_a - 35.85)^2 \tag{4c}$$

The saturation vapor pressure is related to air temperature T_a (K):

$$e_s = 0.6108 \cdot \exp\left(17.27(T_a - 273.15) / (T_a - 35.85)\right) \tag{4d}$$

The actual vapor pressure is positive to air humidity RH (%):

$$e_a = RH \cdot e_s / 100 \tag{4e}$$

The psychrometric constant is calculated by:

$$\gamma = C_{p-a} \cdot P_{at} / (L \cdot r_{mw}) \tag{4f}$$

where P_{at} is the atmospheric pressure (Pa), r_{mw} is the molecular weight of water vapor to dry air.

The crop canopy resistance is:

$$r_c = r_1 / (0.5 \cdot LAI) \tag{4g}$$

where r_1 is the stomatal resistance of a single leaf (sm^{-1}), LAI is the leaf area index [26,35]:

(a) For clipped grass (h_c = 0.05 - 0.15 m):

$$LAI = 24 \cdot h_c \tag{4h}$$

(b) For other crops:

$$LAI = 5.5 + 1.5 \ln(h_c) \tag{4i}$$

2.2 Soil surface water balance

The precipitation (P) is the only water source, which is kept balanced with water run off (W_r), actual evaporation (E), and infiltration (W_i) through the land surface [36]. Therefore:

$$P = W_r + E + W_i \tag{5}$$

2.3 Hydrothermal transfer in subsurface soil

The Richards equation is used to calculate the hydraulic variation with space and time:

$$\rho_w \cdot \psi \cdot \frac{\partial H_p}{\partial t} + \nabla \cdot \left[-K \cdot k_r \cdot \nabla \cdot \rho_w \cdot \left(H_p + D + H_k \right) \right] = 0 \tag{6}$$

where ρ_w is the water density (kgm^{-3}), ψ is the specific moisture capacity (m^{-1}), H_p is the suction head (m), t is the time (s), K is the hydraulic conductivity (ms^{-1}), k_r is the relative hydraulic conductivity, D is the elevation head (m), H_k is the kinetic head (m). The kinetic head is very small in the current investigation and it is therefore neglected.

Mualem equation [37] is used for obtaining relative hydraulic conductivity:

$$k_r = \begin{cases} S_e^{\,l} \left[1 - \left(1 - S_e^{\,n/(n-1)} \right)^{1-1/n} \right]^2 & H_p < 0 \\ 1 & H_p \geq 0 \end{cases} \tag{7}$$

where S_e is the relative saturation of the soil, l is the pore connectivity parameter, n is a measure of the pore-size distribution.

van Genuchten [38] equation is used for representing the relation between the suction and the relative saturation:

$$S_e = \begin{cases} \dfrac{1}{\left[1 + \left| \alpha H_p \right|^n \right]^{1-1/n}} & H_p < 0 \\ 1 & H_p \geq 0 \end{cases} \tag{8}$$

where α is related to the inverse of the air entry suction (m^{-1}).

The approach proposed by Nowamooz et al. [39,40] is used for the soil thermal conductivity:

$$k_s = (0.443x_s + 0.081\gamma_d)\frac{(4.4x_s + 0.4)S_r}{1 + (4.4x_s - 0.6)\mathrm{S}_r} + 0.087x_s + 0.019\gamma_d \quad (9)$$

where x_s, γ_d, and S_r are the soil sand content, dry unit weight (kNm^{-3}) and saturation, respectively.

The approach proposed by Tang and Nowamooz [41,42] is used to calculate the soil volumetric heat capacity:

$$C_{v-s} = (4.18 - 0.095\gamma_d - 0.3x_s)\mathrm{S}_r + 0.09\gamma_d - 0.2x_s \quad (10)$$

The energy conservation equation in the soil is given as:

$$\rho_s C_{p-s}\frac{\partial T_s}{\partial t} = \nabla\cdot(k_s\nabla T_s) + \nabla\cdot\left(\rho_w C_{p-w}u_w T_s\right) + Q_s \quad (11)$$

where ρ_s is the soil density (kgm^{-3}), $C_{p\text{-}s}$ is the soil heat capacity ($Jkg^{-1}K^{-1}$), T_s is the soil temperature (°C), $C_{p\text{-}w}$ is the water specific heat capacity ($Jkg^{-1}K^{-1}$), u_w is the water velocity in soil (ms^{-1}), Q_s is the soil heat source (Wm^{-3}).

The hydrothermal transfer equations in subsurface soil have been introduced in detail in our previous publication [42].

2.4 Heat transfer in pipe

The 1D heat transfer in the pipe includes its wall layer, its internal film, and the carrying incompressible fluid. The friction heat is kept in the energy balance equation although it has a negligible effect in the heat transfer of the pipe. The energy conservation equation is given as:

$$A\rho_f C_{p-f}\frac{\partial T_f}{\partial t} + A\rho_f C_{p-f}u_f\cdot\nabla T_f = \nabla\cdot Ak_f\nabla T_f + f_D\frac{\rho_f A}{2d_h}\left|u_f\right|u_f{}^2 + Q_{wall} \quad (12)$$

where A is the pipe inner cross-sectional area (m^2), ρ_f is the fluid density (kgm^{-3}), $C_{p\text{-}f}$ is the fluid specific heat capacity ($Jkg^{-1}K^{-1}$), T_f is the fluid temperature (°C), u_f is the fluid flowing velocity (ms^{-1}), k_f is the fluid thermal conductivity ($Wm^{-1}K^{-1}$), f_D is the Darcy friction factor,

d_h is the hydraulic diameter (m) and Q_{wall} is the energy from the surrounding media (Wm^{-1}). The energy from the surrounding media is given as:

$$Q_{wall} = h_{\text{int}} \cdot Z \cdot (T_{i-p} - T_f) \tag{13}$$

where h_{int} is the film heat transfer coefficient ($Wm^{-2}K^{-1}$). Z is the pipe inner perimeter (m) and $T_{i\text{-}p}$ is the inner pipe temperature (°C).

3. Validation of the proposed numerical framework

The atmosphere-soil-HGHE interaction is considered in our numerical simulation framework. To evaluate the capacity of the proposed model, the atmosphere-soil interaction (equations 1-11) was firstly evaluated by using a local instrumented temperature probe [43]. Subsequently, the soil-HGHE interaction (equations 11-13) was evaluated by an indoor experiment conducted by Yoon et al. [44].

3.1 Validation for the atmosphere-soil interaction

A local site in Alsace region (France) was chosen for this validation since we have access to the geological, metrological and hydraulic conditions of this field [39,42,43]. The soil at the top 20 m is constituted of 4 soils and 6 soil layers (Fig. 2): layer 1 with 0.1 m of clay loam; layer 2 with 1 m of sandy loam; layer 3 with 0.15 m of loam; layer 4 with 4.75 m of sandy loam; layer 5 with 8 m of a second sandy loam and layer 6 with 6 m of loam.

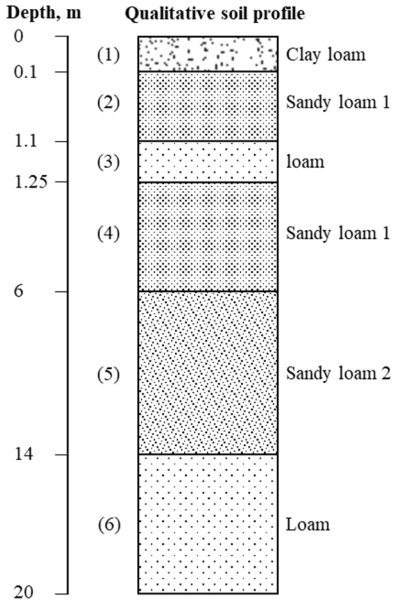

Fig. 2 Six soil layers at the investigated site.

A temperature probe was installed at a depth of 1.03 m on this site. To validate the capacity of the model for the atmosphere-soil interaction, the model was run for three years without the installation of the HGHE.

Table 1 and Table 2 present the parameters for the atmosphere-soil interaction (equations 1-11). Table 1 presents the parameters for the soil surface energy balance and Table 2 summarizes the hydrothermal properties of the subsurface soils [42,45].

Table 1 Parameters for the soil surface energy balance

Parameter	Description	Value	Unit
a_l	Albedo	0.25	-
ε	Soil emissivity	0.97	-
σ	Stephan-Boltzman constant	5.67×10^{-8}	$Wm^{-2}K^{-4}$
ρ_a	Air density	1.25	kgm^{-3}
$C_{p\text{-}a}$	Air specific heat capacity	1.003×10^{3}	$Jkg^{-1}K^{-1}$
z_m	Height to collect the meteorological data	2	m
h_c	Grass height	0.06	m
κ	von Karman constant	0.41	-
L	Latent heat of vaporization	2.260	Jkg^{-1}
P_{at}	Atmospheric pressure	102000	Pa

r_{mw}	Molecular weight of water vapor to dry air	0.622	-
r_l	Stomatal resistance of a single leaf	100	sm^{-1}

Table 2 Hydrothermal properties of the subsurface soils

Material	K (ms^{-1})	l (-)	α (m^{-1})	n (-)	θ_s (-)	θ_r (-)	x_s (-)	γ_s (kNm^{-3})	γ_d (kNm^{-3})
Clay loam	1.53E-6	0.5	1.99	1.22	0.50	0.03	0.35	27.0	13.5
Sandy loam 1	1.78E-5	0.5	2.60	1.52	0.39	0.02	0.80	26.2	16.0
Loam	2.19E-6	0.5	2.35	1.38	0.47	0.02	0.50	26.8	14.2
Sandy loam 2	1.45E-5	0.5	2.48	1.50	0.40	0.02	0.60	26.7	16.0

The ambient temperatures of the investigated site have been monitored during several years [43,46]. Based on the in-situ measurements, the following equation is used for approximating ambient temperature [43,46]:

$$T_a = 13.4\text{-}9.43\cdot\sin(2\cdot\pi/(365\times24\times3600)\cdot t\text{+}4.63)+ (\text{-}3.52\text{+}2.1\times\sin(2\cdot\pi/(365\times24\times3600)\cdot \text{t-}1.25))\cdot\sin(2\cdot\pi/(24\times3600)\cdot \text{t+}1) \quad (14)$$

where t is time (s). The comparison between the approximated and measured ambient temperatures from July 2014 to July 2017 is shown in Fig. 3:

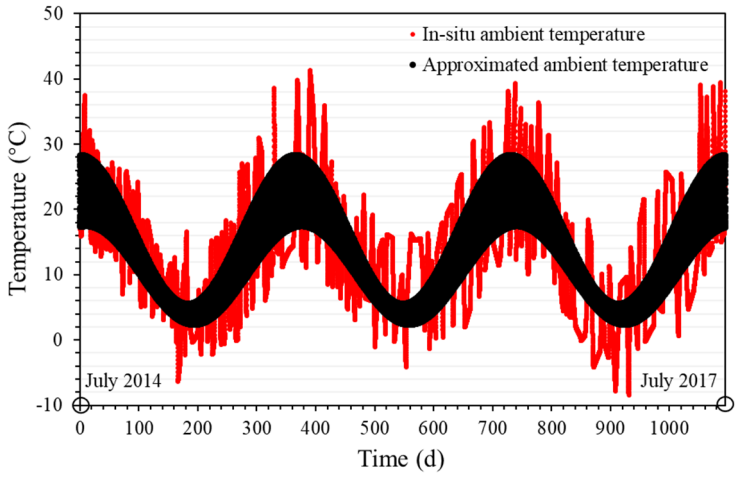

Fig. 3 Comparison between the approximated and measured ambient temperatures for a duration of 3 years from July 2014 to July 2017 [43,46].

Moreover, the local shortwave radiation is given as:

$$R_s = 130 + 80\cdot\cos(2\cdot\pi/(365\times3600\times24)\cdot t) \quad (15)$$

At the site, there is no obvious seasonal fluctuation of cloud cover, wind speed, precipitation and air humidity with time. Therefore, an average cloud cover of 0.41, an average wind speed of 2 ms^{-1}, an average monthly precipitation of 55.7 mm, and an average air humidity of 83% are applied in the numerical simulation model to capture the main meteorological condition of the local site.

For the surface water balance, 20% of precipitation run off, and the other 80% participate into evapotranspiration or infiltration.

Table 3 summarizes all the imposed hydrothermal boundary conditions in this part. The temperature gradient at the bottom boundary is set 0.142 Km^{-1} [47], and the extra water from the precipitation is drained at the bottom boundary. The groundwater level is set constant at the depth of 7.5 m in the whole year. No hydrothermal flow is imposed on the lateral boundaries.

Table 3 Hydrothermal boundary conditions for the scenario with the atmosphere-soil interaction

Surface	Hydraulic condition, value (unit)	Thermal condition, value (unit)
Top	Neumann, equation 5 (ms^{-1})	Neumann, equation 1 (Wm^{-2})
Lateral	Adiabatic, -	Adiabatic, -
Bottom	Dirichlet, model height – groundwater level (m)	Neumann, bottom temperature gradient × bottom soil thermal conductivity (Wm^{-2})

An equilibrium method is used to obtain the initial hydrothermal profiles [42,45]. Fig. 4 shows the suction and temperature profiles derived from this approach.

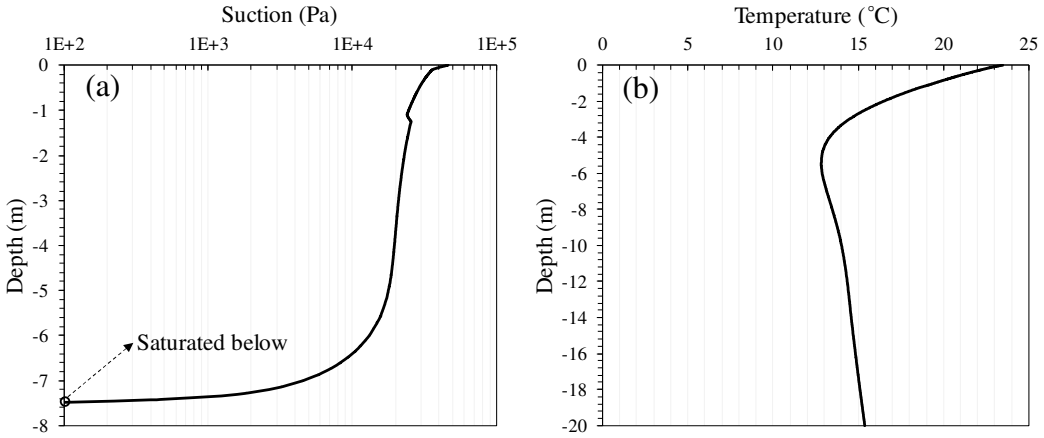

Fig. 4 Initial hydrothermal profiles: (a) suction profile and (b) temperature profile.

After the obtention of the initial suction profile, the corresponding initial profiles for the volumetric water content (Fig. 5-a), the soil thermal conductivity (Fig. 5-b) and the soil volumetric heat capacity (Fig. 5-c) are deduced by using the equations 8-10 and their parameters reported in Table 2.

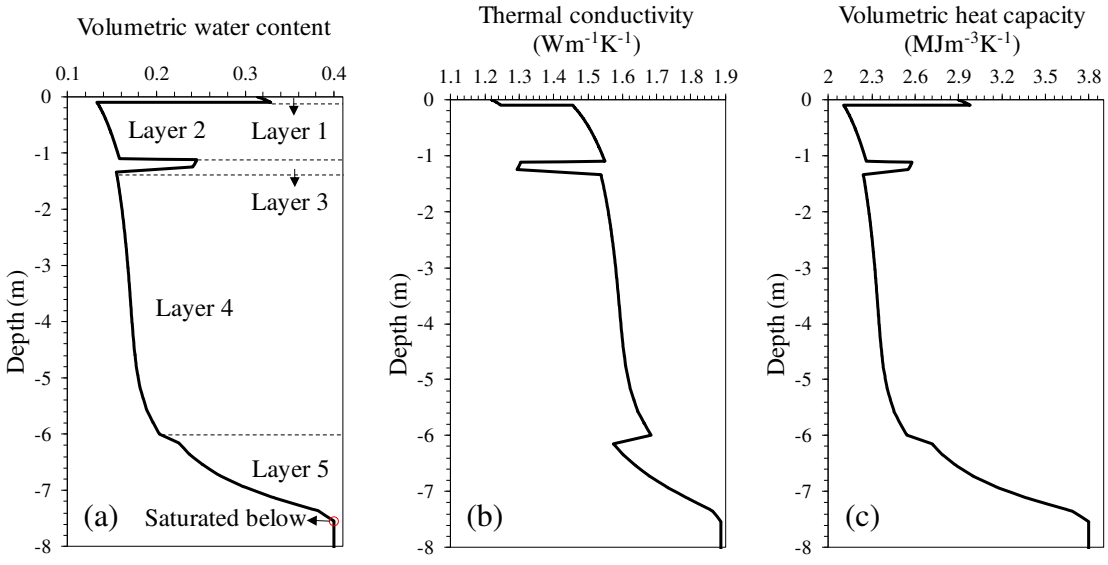

Fig. 5 Initial hydrothermal profiles deduced from the initial suction profile: (a) volumetric water content profile; (b) thermal conductivity profile and (c) volumetric heat capacity profile.

Fig. 6 shows the comparison of the numerical prediction for a duration of 3 years from July 2014 to July 2017. The Root-Mean-Square Error (RMSE) is determined by:

$$\mathrm{RMSE} = \left[\sum_{i=1}^{N} (T_{np,i} - T_{im,i})^2 / N \right]^{1/2} \quad (16)$$

where T_{np} is the temperature (°C) from the numerical prediction, T_{im} is the temperature (°C) from the in-situ measurement, N is the number of temperature data. The comparison shows that the numerical framework is capable to predict the soil temperature with the RMSE value of 1.6 °C.

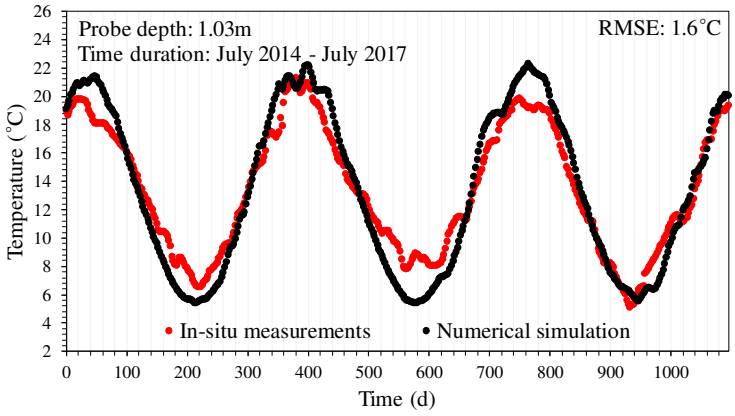

Fig. 6 Comparison between the numerical predictions and the in-situ measurements [43] for 3 years (from July 2014 to July 2017).

3.2 Validation for the soil-HGHE interaction

The soil-HGHE interaction of the proposed numerical framework is evaluated by an indoor experiment reported by Yoon et al. [44]. In their work, two experiments are conducted in a sandy box for slinky-type HGHEs with pipe lengths of 24 and 66 m. They have further used a far-infrared radiation heater to maintain constant the indoor temperature. In their experiment, a polybutylene pipe with inner and outer diameters of 16 and 20 mm is installed at the depth of 0.5 m in a sand box. The sand box has a length of 5 m, a width of 1 m and a depth of 1 m. The surrounding dry sand has a thermal conductivity of 0.26 $\mathrm{Wm^{-1}K^{-1}}$, specific heat capacity of 785 $\mathrm{Jkg^{-1}K^{-1}}$ and a density of 1.397 $\mathrm{gcm^{-3}}$. The carrying fluid is water with a velocity of 0.3921 $\mathrm{ms^{-1}}$ [10]. The initial box temperature is between 17 and 18 °C. The time duration is

30 h for the two experiments. Table 4 summarizes the imposed thermal boundary conditions for this indoor experiment. Water transfer in soil is not considered in this experiment.

Table 4 Thermal boundary condition for the indoor experiment reported by Yoon et al. [44]

Surface or element	Thermal condition, value (unit)
Top	Dirichlet, 17.5 (°C)
Lateral	Adiabatic, -
Bottom	Adiabatic, -
HGHE inlet	Dirichlet, time-varying values [44] (K)

Fig. 7 shows the comparison of the carrying fluid outlet temperatures between the in-situ measurements and the numerical predictions. A good correspondence between the experiment and prediction proves that the established numerical model considers appropriately the soil-HGHE interaction in its framework.

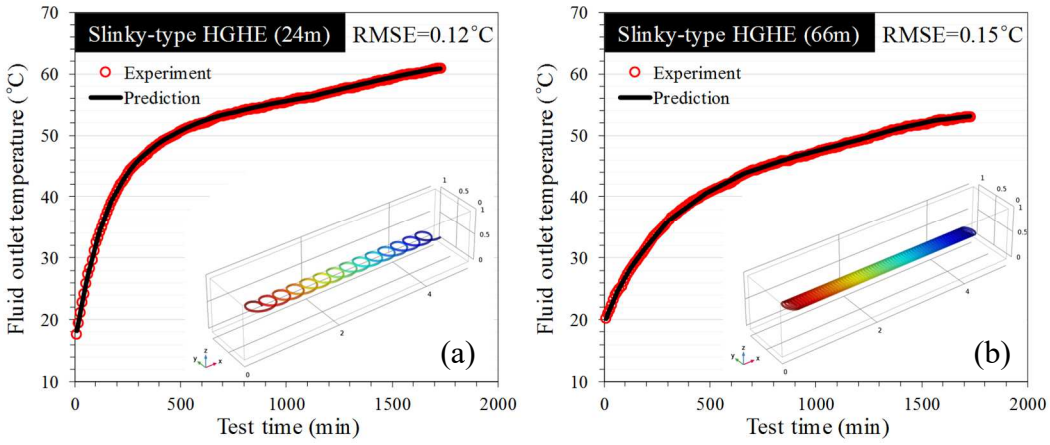

Fig. 7 The comparison between the experiment and the numerical prediction for the carrying fluid outlet temperatures: (a) slinky-type HGHE with a total pipe length of 24 m and (b) slinky-type HGHE with a total pipe length of 66 m.

4 Numerical simulation results with the atmosphere-soil-HGHE interaction

After validating the numerical framework, the simulation results are subsequently presented in this section considering the atmosphere-soil-HGHE interaction. The same site presented in section 3.1 is investigated in this section. To identify the effect of the atmosphere-soil interaction, another scenario is also tested without considering the atmosphere-soil interaction.

4.1 Geometry, mesh and operation options

The studied geometry has a length of 30 m, a width of 12 m and a height of 20 m. This deep geometry was selected to have no hydrothermal impact of the seasonal metrological condition on the bottom boundary. A slinky-type HGHE with 0.03 m of inner diameter and 0.036 m of outer diameter is installed 1 m below surface, covered with the backfill soil (sandy loam 1 presented in section 3.1). The geometry strictly followed the geological profile illustrated in the site description (section 3.1). A swept mesh was deployed to obtain reasonable computation time. It should be noted that the generated meshes are denser in the shallow depths since the shallow ground is more sensitive to hydrothermal fluctuation on the land surface. In addition, the meshes around the HGHE are also denser due to the steep temperature and suction gradients [48]. In total, 75894 meshes were generated for this numerical simulation model. The geometry and its mesh are shown in Fig. 8.

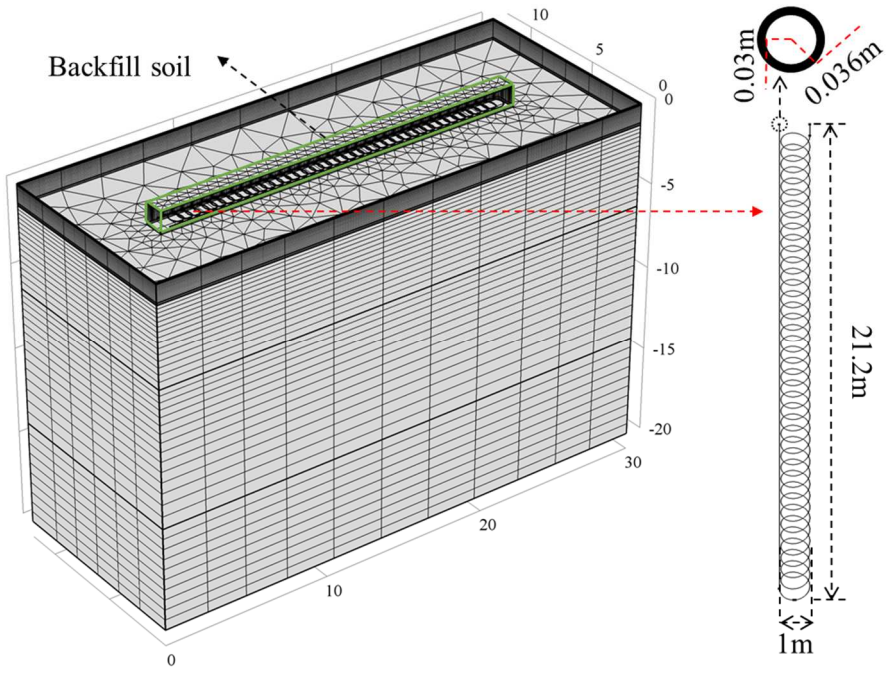

Fig. 8 Geometry and its mesh for the numerical simulations.

The meteorological condition corresponds completely to the local condition presented in section 3.1. The same parameters reported in Tables 1 & 2 are used for the atmosphere-soil interaction. The same aforementioned cloud cover, wind speed, precipitation and air humidity are also applied (section 3.1). The ambient temperatures for three successive years presented in Fig. 3 are approximated for one year in Fig. 9-a. Fig. 9-b presents the shortwave radiation with time for one year derived from equation 15.

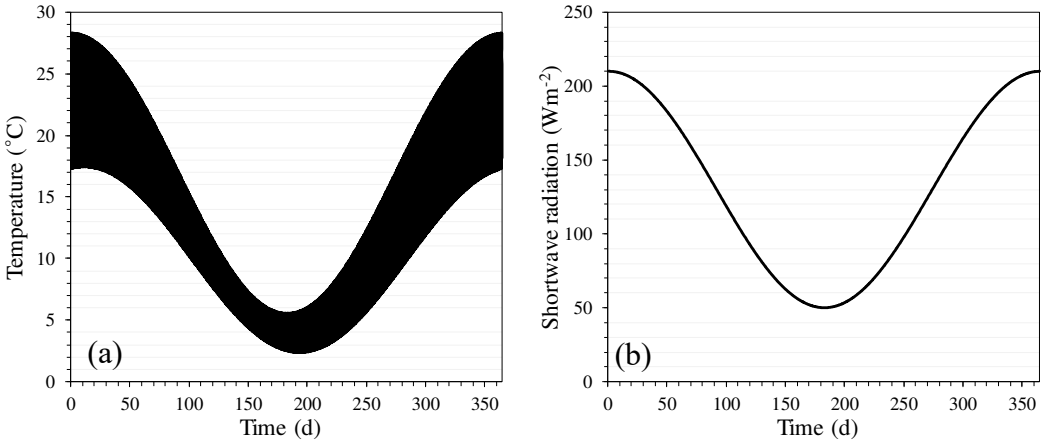

Fig. 9 (a) Ambient temperature fluctuation for one year and (b) shortwave radiation fluctuation for one year.

The pipe is a High-Density Polyethylene (HDPE) pipe with the thermal conductivity of 0.4 $Wm^{-1}K^{-1}$. Propylene Glycol (PG) with a volume concentration of 25% is selected as the carrying fluid. It has a dynamic viscosity of 0.0055 Pas, a density of 1026 kgm^{-3}, a thermal conductivity of 0.45 $Wm^{-1}K^{-1}$ and a specific heat capacity of 3974 $Jkg^{-1}K^{-1}$ [49]. The carrying fluid velocity is 0.5 ms^{-1} during the operation period.

A heating scenario is considered in our simulations according to the local climate condition. The HGHE works from the 100th day to the 265th day in a year. A seasonal heat extraction rate varying from 10 to 40 Wm^{-1} is applied to the HGHE during its operation period (Fig. 10). The time step for the numerical simulation model is 0.5 day.

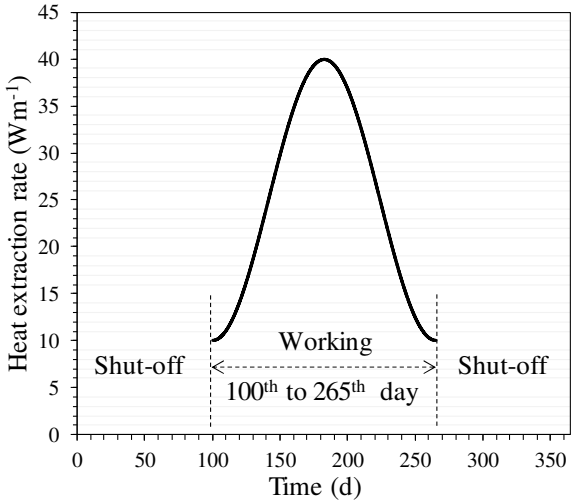

Fig. 10 Heat extraction rate (Wm^{-1}) during the operation period of the HGHE.

4.2 Annual fluctuation of the hydrothermal properties and the HGHE performance

To visualize the spatial and temporal hydrothermal fluctuation in soil, five horizontal line probes are positioned at five different depths: surface (or zero), 1, 2.5, 5 and 10 m (Fig. 11). All the probes are installed in the same vertical plane through the center of the HGHE.

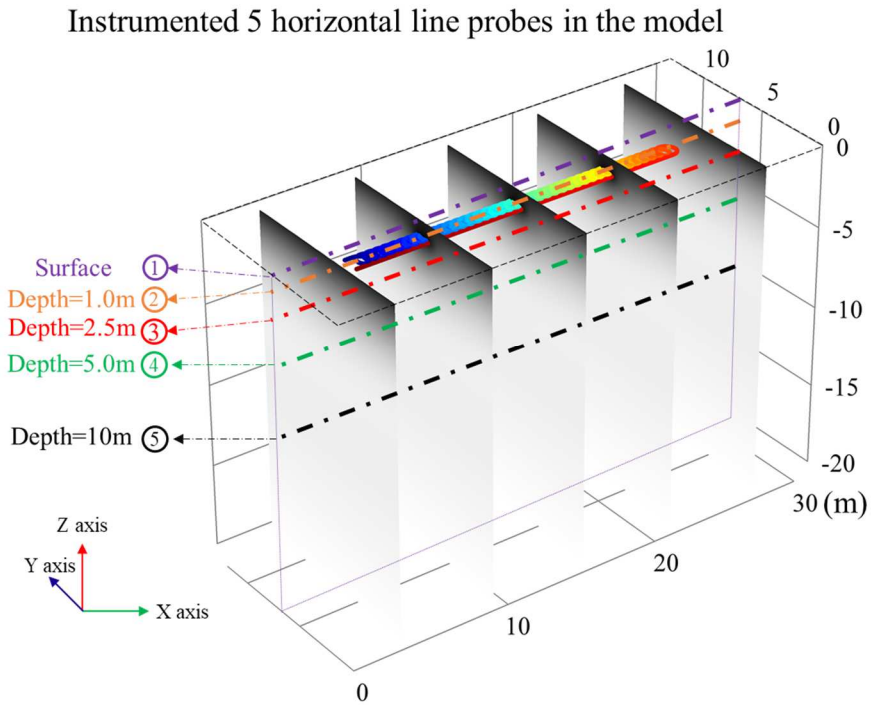

Fig. 11 Five horizontal line probes positioned at different depths: 0, 1, 2.5, 5 and 10 m.

Fig. 12 shows the variation of the volumetric water content (Fig. 12-a) and the temperature (Fig. 12-b) in the 5 probes at different times (99, 130, 182.5, 200 and 260 days). Fig. 12-a shows that the volumetric water content has less fluctuation with time as the depth increases. The fluctuation of volumetric water content becomes negligible as the depth is higher than 5 m. Due to the existence of the backfill soil, the volumetric water content differs spatially along the HGHE, especially on the land surface. The same effect can be observed at the depth of 1.0 m, while it disappears at a depth higher than 2.5 m. Fig. 12-b shows that the seasonal temperature fluctuation is obvious in the shallow depths, while it almost vanishes when the depth reaches 10 m. During the service period, the temperature around the HGHE decreases. The line probe 2 is the most influenced probe because it is positioned at the same depth of the HGHE. The effect is also evident at the depth of 2.5 m. The surface temperature has also been influenced during the service period of the HGHE, and a difference of 0.6 °C is observed after 200 days. The HGHE operation influences less the subsurface temperature when the distance

from the HGHE becomes larger. The soil temperature is negligibly influenced by the HGHE at the depth of 5 m, and this effect can be considered absent at the depth of 10 m.

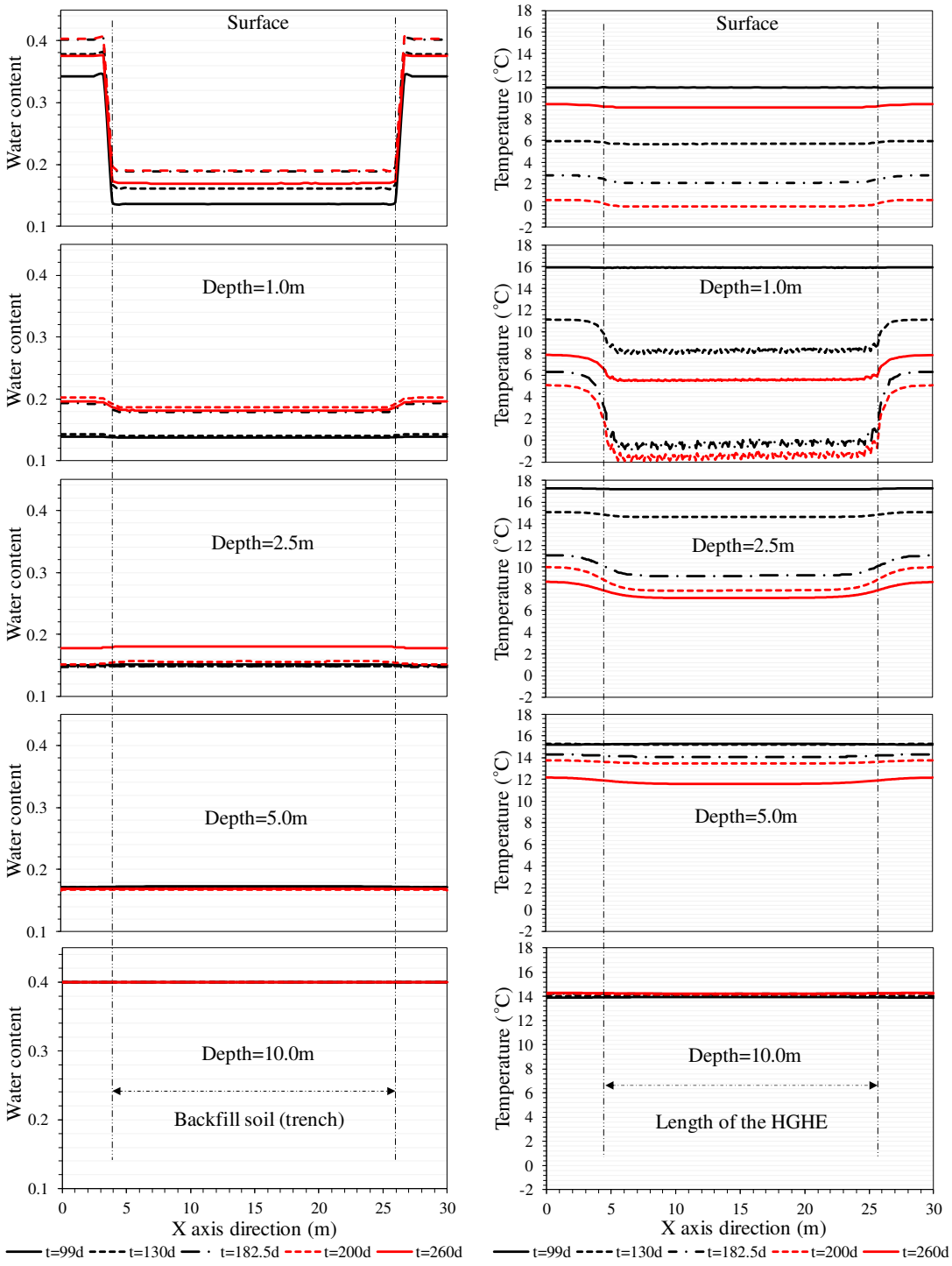

(a) (b)

Fig. 12 Volumetric water content and temperature fluctuation at 5 times of a year for the five

horizontal probes: (a) volumetric water content fluctuation and (b) temperature fluctuation.

The HGHE operation affects the land surface temperature and consequently its ground heat flux. To visualize this effect, the heat flux fluctuation is presented along the surface line probe (probe 1) in Fig. 13. The ground heat flux remains unchanged during the first 99 days. When the HGHE starts working, the ground heat flux at the zone affected by the HGHE is higher than the non-affected zone due to the heat extraction during the heating season. Specifically, the ground heat fluxes at the zone affected by the HGHE are 2.7, 9.2, 8.5 and 2.7 Wm^{-2} higher than the unaffected zone on the days 130, 182.5, 200 and 260, respectively.

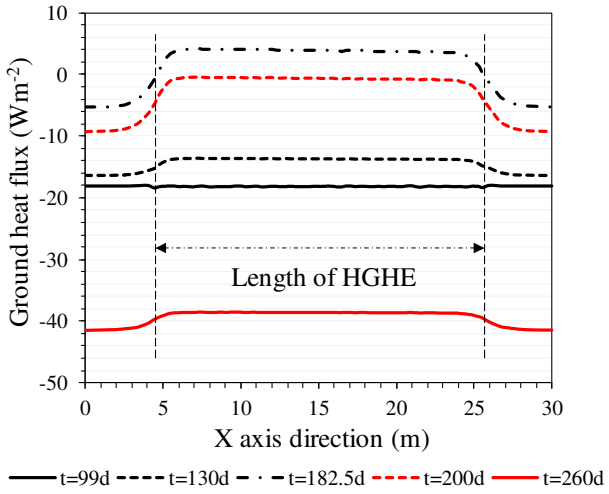

Fig. 13 Ground heat flux fluctuation detected by the horizontal line probe 1 on the land surface.

During the service time of the HGHE, the Total Extracted Energy (TEE) can be obtained by the following equation:

$$\mathrm{TEE} = \int A\rho_f u_f C_{p-f}(T_{out} - T_{in})dt \tag{17}$$

where T_{in} is the fluid inlet temperature (°C).

Fig. 14 shows the TEE and the fluid outlet temperature of the HGHE during its annual working period. The figure shows that the installed HGHE can extract 7.52 GJ of energy after

1 year. The annual average fluid outlet temperature can be obtained as 3.41 °C in the operation period. Generally, the fluid outlet temperature decreases continuously until the day 201, and then it increases until it stops working. The phenomenon illustrates that a time lag of 18.5 days exists between the peak heat load (t = 182.5 d, Fig. 10) and the lowest ground temperature (t = 201 d) surrounding the HGHE.

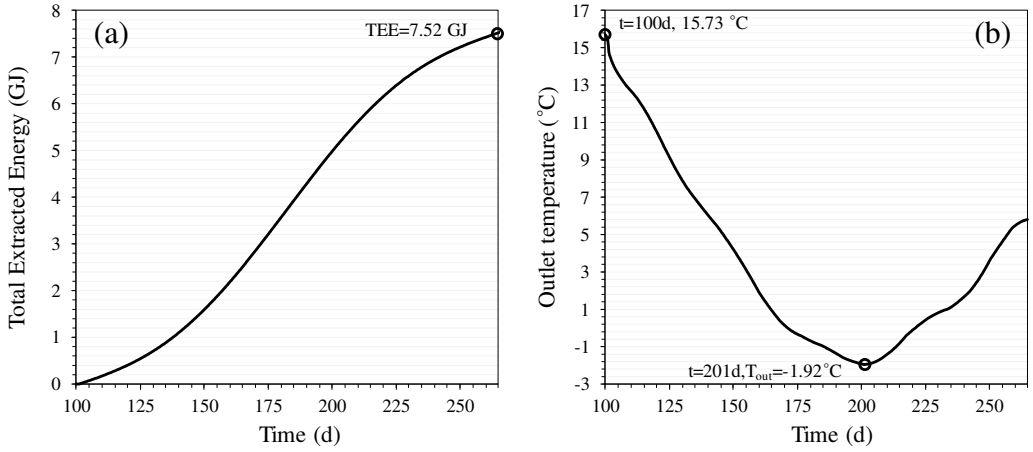

Fig. 14 The extracted energy and the fluid outlet temperature with time during the service period of the HGHE: (a) extracted energy with time and (b) fluid outlet temperature with time.

4.3 The comparison of the HGHE performance at different depths with and without considering the atmosphere-soil interaction

As shown in Fig. 12-b and Fig. 13, the HGHE operation influences simultaneously the land surface temperature and the ground heat flux. To identify this influence on the outlet temperature of the HGHE, another scenario is tested in this part without considering the atmosphere-soil interaction. Compared to the boundary conditions with the atmosphere-soil interaction (Table 3), the popular Dirichlet boundary condition on the land surface is considered in this new scenario (Table 5), where the atmosphere temperature (equation 14) is imposed to the land surface and the operation of the HGHE has no effect on the land surface

temperature and heat flux. In both scenarios, the energy extraction rate (Fig. 10) and the TEE (Fig. 14-b) are kept the same.

Table 5 Hydrothermal boundary conditions for the scenario without the atmosphere-soil interaction

Surface	Hydraulic condition, value (unit)	Thermal condition, value (unit)
Top	Neumann, equation 5 (ms^{-1})	Dirichlet, equation 14 (°C)
Lateral	Adiabatic, -	Adiabatic, -
Bottom	Dirichlet, model height – groundwater level (m)	Neumann, bottom temperature gradient × bottom soil thermal conductivity (Wm^{-2})

Fig. 15 shows the fluid outlet temperatures obtained in both scenarios for the HGHE installed at the depths of 0.5, 1.0, 1.5 and 2 m. The figure shows that the non-consideration of the atmosphere-soil interaction overestimates the fluid outlet temperatures, and this overestimation declines with the increase of the installation depth. When the HGHE is installed at a larger depth, the fluctuation of its outlet temperatures is less significant in both scenarios.

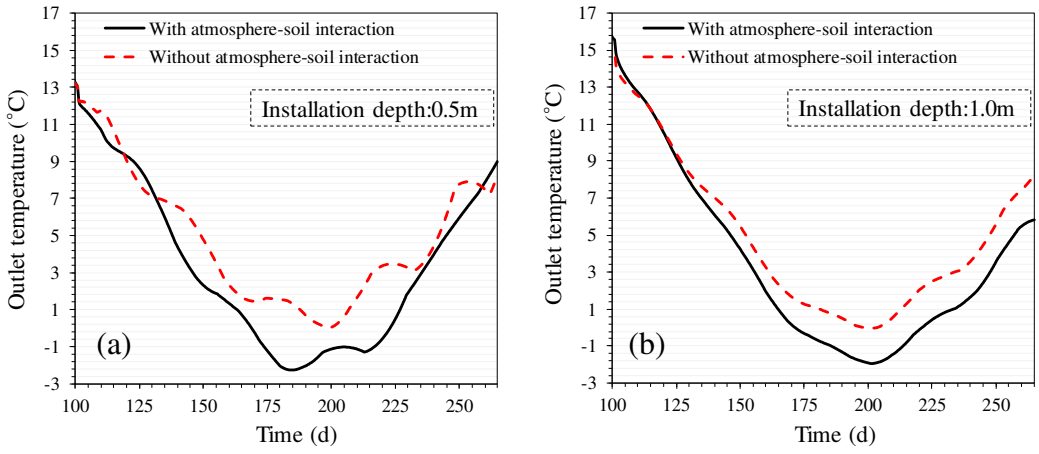

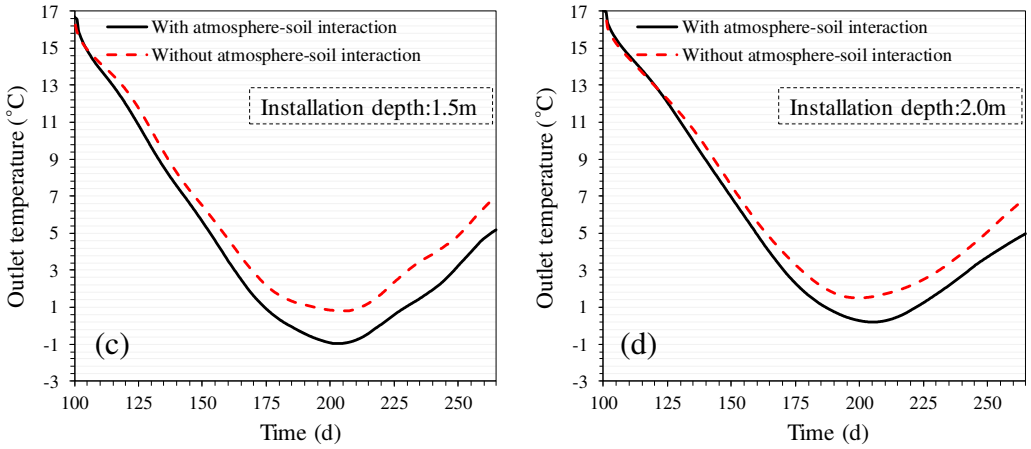

Fig. 15 Carrying fluid outlet temperatures with time regarding with and without the atmosphere-soil interaction for the HGHE installed at 4 different depths: (a) 0.5 m; (b) 1 m; (c) 1.5 m and (d) 2 m.

Fig. 16 compares the annual average fluid outlet temperatures of these 2 scenarios. Generally, a deep installation improves the fluid outlet temperature. When the installation depth increases from 0.5 to 2 m, the annual average fluid outlet temperatures increase 61.11% and 27.56% correspondingly for the scenarios with and without considering the atmosphere-soil interaction. The increase of the installation depth from 0.5 to 1 m has an insignificant effect on the annual average fluid outlet temperatures in both scenarios.

Furthermore, the results confirm the significant influence of the atmosphere-soil interaction in the HGHE simulations. The annual average fluid outlet temperatures are highly overestimated when the interaction is absent in the calculations especially if the HGHE is installed close to the land surface. The overestimation caused by the non-consideration of the atmosphere-soil interaction decreases with the increase of the installation depth. In general, the overestimation decreases from 47.99% to 17.16% as the installation depth increases from 0.5 to 2 m.

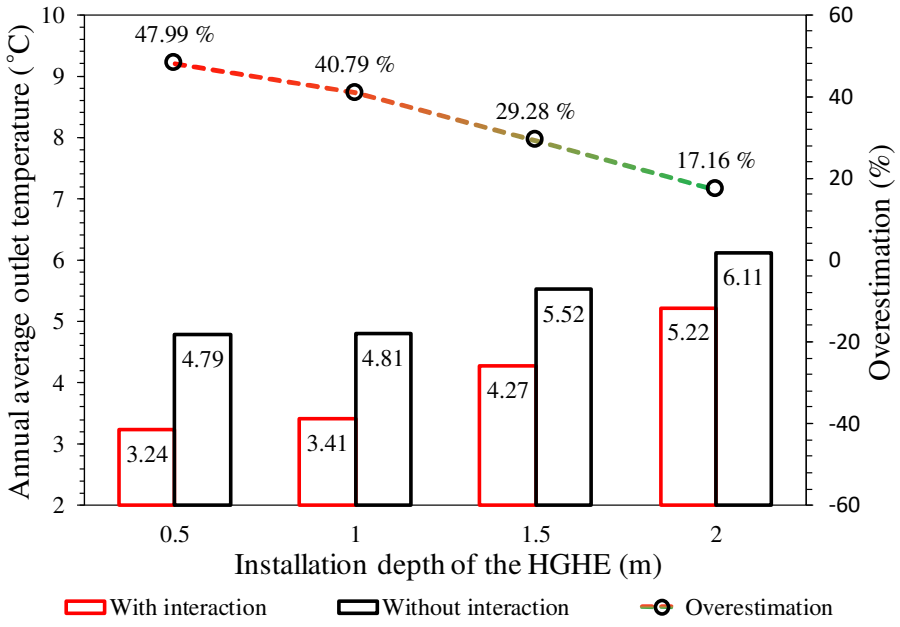

Fig. 16 Comparison between the annual average fluid outlet temperatures with and without the atmosphere-soil interaction.

As it has been reported regularly in the literature [49,50,51], the fluid outlet temperature from the HGHE is linear to the heat pump performance, and consequently the HGHE performance. The higher the fluid outlet temperature in the heating scenario, the higher the HGHE performance. Therefore, the same conclusions observed for the fluid outlet temperature can be generalized for the HGHE performance.

5 Conclusion

This paper has evaluated the outlet temperatures of a slinky-type HGHE installed in a multi-layered soil field by considering the local metrological and geological conditions.

The numerical simulations were firstly validated by the measured data from literature. The results showed the good capacity of the proposed framework to consider the atmosphere-soil-HGHE interaction.

The yearly variations of the in-situ hydrothermal properties were investigated on the

horizontal line probes positioned at 5 different depths. The results showed that the soil surface temperature and the ground heat flux were obviously affected during the service period of the HGHE. The affected surface zone had lower temperatures than the unaffected zone while a higher ground heat flux was observed in this zone. Subsequently, the annual average fluid outlet temperature for the in-situ site was estimated 3.41 °C under the seasonal heat load.

Moreover, the fluid outlet temperatures were further compared for the HGHE installed at 4 different depths with and without considering the atmosphere-soil interaction. Generally, a deep installation increased the fluid outlet temperatures; however, this increase was insignificant when the installation depth increased from 0.5 to 1 m. The results also showed the importance of considering atmosphere-soil interaction in the numerical calculations. The annual average fluid outlet temperature was overestimated when the atmosphere-soil interaction was not considered. This overestimation decreased from 47.99% to 17.16% as the installation depth of the HGHE increased from 0.5 to 2 m.

These findings are important in the design stage of the HGHE engineering. The effect of the atmosphere-soil interaction on the HGHE performance is a crucial factor. This effect is more /less intensified when the installation depth decreased/increased. A deep installation of the HGHE improves the system performance, but it increases the trench digging cost. An appropriate cost/performance ratio may be the best practical solution in HGHE engineering.

Acknowledgment

The authors are grateful to China Scholarship Council (CSC) for providing the financial support.

Reference

[1] Shortall R, Davidsdottir B, Axelsson G. Geothermal energy for sustainable development: A review of sustainability impacts and assessment frameworks. Renewable and

Sustainable Energy Reviews 2015; 44: 391–406. https://doi.org/10.1016/j.rser.2014.12.020.

[2] Sangi R, Müller D. Dynamic modelling and simulation of a slinky-coil horizontal ground heat exchanger using Modelica. Journal of Building Engineering 2018; https://doi.org/10.1016/j.jobe.2018.01.005.

[3] Lee C, You J, Park H. In-situ response test of various borehole depths and heat injection rates at standing column well geothermal heat exchanger systems. Energy & Buildings; 2018; 172: 201–208. https://doi.org/10.1016/j.enbuild.2018.05.009.

[4] Florides G, Kalogirou S. Ground heat exchangers-A review of systems, models and applications. Renewable Energy 2007. 32: 2461–2478. https://doi.org/10.1016/j.renene.2006.12.014.

[5] Adamovsky D, Neuberger P, Adamovsky R. Changes in energy and temperature in the ground mass with horizontal heat exchangers-The energy source for heat pumps. Energy and Buildings 2015. 92: 107-115. https://doi.org/10.1016/j.enbuild.2015.01.052.

[6] Self S, Reddy B, Rosen M. Geothermal heat pump systems: Status review and comparison with other heating options. Applied Energy 2013; 101: 341–348. https://doi.org/10.1016/j.apenergy.2012.01.048.

[7] Xiong Z, Fisher D, Spitler J. Development and validation of a Slinky™ ground heat exchanger model. Applied Energy 2015; 141: 57–69. https://doi.org/10.1016/j.apenergy.2014.11.058.

[8] Al-Ameen Y, Ianakiev A, Evans R. Recycling construction and industrial landfill waste material for backfill in horizontal ground heat exchanger systems. Energy 2018; 151: 556-568. https://doi.org/10.1016/j.energy.2018.03.095.

[9] Gonzalez R, Verhoef A, Vidale P, Main B, Gan G, Wu Y. Interactions between the physical soil environment and a horizontal ground coupled heat pump, for a domestic site in the UK. Renewable Energy 44 (2012) 141-153. https://doi.org/10.1016/j.renene.2012.01.080.

[10] Habibi M, Hakkaki-Fard A. Evaluation and improvement of the thermal performance of different types of horizontal ground heat exchangers based on techno-economic analysis. Energy Conversion and Management 2018; 171: 1177-1192. https://doi.org/10.1016/j.enconman.2018.06.070.

[11] Kim J, Lee S, Yoon S, Go G. Thermal performance evaluation and parametric study of a horizontal ground heat exchanger. Geothermics 2016; 60: 134-143. https://doi.org/10.1016/j.geothermics.2015.12.009.

[12] Congedo P, Colangelo G, Starace G. CFD simulations of horizontal ground heat exchangers: A comparison among different configurations. Applied Thermal Engineering 33-34 (2012) 24-32. https://doi.org/10.1016/j.applthermaleng.2011.09.005.

[13] Gan G. Dynamic thermal modelling of horizontal ground-source heat pumps. International Journal of Low-Carbon Technologies 2013; 8: 95-105. doi:10.1093/ijlct/ctt012.

[14] Go G, Lee S, Yoon S, Kim M. Optimum design of horizontal ground-coupled heat pump

systems using spiral-coil-loop heat exchangers. Applied Energy 2016; 162: 330-345. https://doi.org/10.1016/j.apenergy.2015.10.113.

[15] Selamat S, Miyara A, Kariya K. Numerical study of horizontal ground heat exchangers for design optimization. Renewable Energy 2016; 95: 561-573. http://dx.doi.org/10.1016/j.renene.2016.04.042.

[16] Li C, Mao J, Zhang H, Xing Z, Li Y, Zhou J. Numerical simulation of horizontal spiral-coil ground source heat pump system: Sensitivity analysis and operation characteristics. Applied Thermal Engineering 2017; 110: 424–435. http://dx.doi.org/10.1016/j.applthermaleng.2016.08.134.

[17] Gao Y, Fan R, Li H, Liu R, Lin X, Guo H, Gao Y. Thermal performance improvement of a horizontal ground-coupled heat exchanger by rainwater harvest. Energy and Buildings 2016; 110: 302-313. http://dx.doi.org/10.1016/j.enbuild.2015.10.030.

[18] Jeon J, Lee S, Kim M, Yoon S. Suggestion of a Scale Factor to Design Spiral-Coil-Type Horizontal Ground Heat Exchangers. Energies 2018; 11:2736. doi:10.3390/en11102736.

[19] Kim M, Lee S, Yoon S, Jeon J. Evaluation of geometric factors influencing thermal performance of horizontal spiral-coil ground heat exchangers. Applied Thermal Engineering 2018; 144: 788–796. https://doi.org/10.1016/j.applthermaleng.2018.08.084.

[20] Han C, Ellett K, Naylor S, Yu X. Influence of local geological data on the performance of horizontal ground-coupled heat pump system integrated with building thermal loads. Renewable Energy 2017; 113: 1046-1055. https://doi.org/10.1016/j.renene.2017.06.025.

[21] Pu L, Xu L, Qi D, Li Y. Structure optimization for horizontal ground heat exchanger. Applied Thermal Engineering 2018; 136: 131–140. https://doi.org/10.1016/j.applthermaleng.2018.02.101.

[22] Wu Y, Gan G, Verhoef A, Vidale P, Gonzalez R. Experimental measurement and numerical simulation of horizontal-coupled slinky ground source heat exchangers. Applied Thermal Engineering 30 (2010) 2574-2583. https://doi.org/10.1016/j.applthermaleng.2010.07.008.

[23] Naylor S, Ellett K, Gustin A. Spatiotemporal variability of ground thermal properties in glacial sediments and implications for horizontal ground heat exchanger design. Renewable Energy 2015; 81: 21-30. https://doi.org/10.1016/j.renene.2015.03.006.

[24] Gan G. Dynamic thermal performance of horizontal ground source heat pumps - The impact of coupled heat and moisture transfer. Energy 2018; 152: 877-887. https://doi.org/10.1016/j.energy.2018.04.008.

[25] Fujii H, Okubo H, Cho, K. Ohyama. Field tests of horizontal ground heat exchangers, in: Proceedings of the 2010 World Geothermal Congress, Bali, Indonesia, April 25-29, 2010, Paper No. 2904, p. 6.

[26] Chalhoub M, Bernier M, Coquet Y, Philippe M. A simple heat and moisture transfer model to predict ground temperature for shallow ground heat exchangers. Renewable Energy 2017; 103: 295-307. http://dx.doi.org/10.1016/j.renene.2016.11.027.

[27] Cole R. The longwave radiation incident upon the external surface of buildings. Building Services Engineers 1976; 44: 195–206.

[28] Choi W, Ooka R, Nam Y. Impact of long-term operation of ground-source heat pump on subsurface thermal state in urban areas. Sustainable Cities and Society 2018; 38: 429-439. https://doi.org/10.1016/j.scs.2017.12.036.

[29] Allen R. A Penman for all seasons. J. Irrig. Drain. Eng. 1986; 112: 348-368.

[30] Turc L. Le Bilan d'eau des sols : relations entre les précipitations, l'évaporation et l'écoulement. Ann. Agron. 1954; 5: 491–569.

[31] Pike J. The estimation of annual runoff from meteorological data in a tropical climate. Journal of Hydrology 1964. 2: 116-123.

[32] Chen X, Buchberger S. Exploring the relationships between warm-season precipitation, potential evaporation, and "apparent" potential evaporation at site scale. Hydrol. Earth Syst. Sci. 2018, 22: 4535–4545. https://doi.org/10.5194/hess-22-4535-2018.

[33] Gerrits A, Savenije H, Veling E, Pfister L. Analytical derivation of the Budyko curve based on rainfall characteristics and a simple evaporation model. Water Resource Research 2009, doi:10.1029/2008WR007308.

[34] Monteith J. Evaporation and environment. Symp. Soc. Exp. Biol 1965; 19: 205-234.

[35] Allen R, Jensen M, Wright J, Burman R. Operational estimates of evapotranspiration. Agron. J. 1989; 81: 650-662.

[36] Dietrich O, Fahle M, Seyfarth M. Behavior of water balance components at sites with shallow groundwater tables: Possibilities and limitations of their simulation using different ways to control weighable groundwater lysimeters. Agricultural Water Management 2016; 163: 75-89. https://doi.org/10.1016/j.agwat.2015.09.005.

[37] Mualem Y. A new model for predicting the hydraulic conductivity of unsaturated porous media. Water Resour. Res. 1976; 12(3): 513-522. https://doi.org/10.1029/WR012i003p00513.

[38] van Genuchten MT. A closed-form equation for predicting the hydraulic conductivity of unsaturated soils. Soil Sci Soc Am J 1980; 44: 892-898. doi: 10.2136/sssaj1980.03615995004400050002x.

[39] Nowamooz H, Nikoo-Sokhan S, Lin J, Chazallon C. Finite difference modeling of heat distribution in multilayer soils with time-spatial hydrothermal properties. Renewable Energy 2015; 76: 7-15. https://doi.org/10.1016/j.renene.2014.11.008.

[40] Nikoosokhan S, Nowamooz H, Chazallon C. Effect of texture, water content and dry density on the soil thermal conductivity. International Journal of Geomechanics and Geoengineering 2016. 11(2): 149-158. https://doi.org/10.1080/17486025.2015.1048313.

[41] Tang F, Nowamooz H. Hydro-thermal properties of the unsaturated soil. Conference: Civil Infrastructures Confronting Severe Weathers and Climate Changes Conference 2019; DOI: 10.1007/978-3-319-95744-9_2.

[42] Tang F, Nowamooz H. Long-term performance of a shallow borehole heat exchanger installed in a geothermal field of Alsace region. Renewable Energy 2018; 128: 210-222. https://doi.org/10.1016/j.renene.2018.05.073.

[43] Lin J, Nowamooz H, Braymand S, Wolff P, Fond C. Impact of soil moisture on the long-

term energy performance of an earth-air heat exchanger system. Renewable Energy 2018; 1-12. https://doi.org/10.1016/j.renene.2018.06.106.

[44] Yoon S, Lee S, Go G. Evaluation of thermal efficiency in different types of horizontal ground heat exchangers. Energy and Buildings 2015; 105: 100-105. http://dx.doi.org/10.1016/j.enbuild.2015.07.054.

[45] Tang F, Nowamooz H. Factors influencing the performance of shallow Borehole Heat Exchanger. Energy Conversion and Management 2019; 181:571-583. https://doi.org/10.1016/j.enconman.2018.12.044.

[46] Cuny M, Lin J, Siroux M, Fond C. Simplification of boundary conditions of the modeling of shallow geothermal systems. French Thermal Congress 2015; La Rochelle, France.

[47] Baillieuxm P, Schill E, Edel J, Mauri G. Localization of temperature anomalies in the Upper Rhine Graben: insights from geophysics and neotectonic activity. International Geology Review 2013; 55: 1744-1762. https://doi.org/10.1080/00206814.2013.794914.

[48] Choi W, Ooka R. Effect of disturbance on thermal response test, part 2: Numerical study of applicability and limitation of infinite line source model for interpretation under disturbance from outdoor environment. Renewable Energy 2016; 85: 1090-1105. http://dx.doi.org/10.1016/j.renene.2015.07.049.

[49] Casasso A, Sethi R. Efficiency of closed loop geothermal heat pumps: a sensitivity analysis. Renew Energy 2014; 62:737-746. https://doi.org/10.1016/j.renene.2013.08.019.

[50] Hein P, Kolditz O, Görke UJ, Bucher A, Shao H. A numerical study on the sustainability and efficiency of borehole heat exchanger coupled ground source heat pump systems. Applied Thermal Engineering 2016; 100: 421-433. https://doi.org/10.1016/j.applthermaleng.2016.02.039.

[51] Shao H, Hein P, Sachse A, Kolditz O. Geoenergy Modeling II: Shallow Geothermal Systems. Springer briefs in energy: computational modeling of energy systems; 2016. https://doi.org/10.1007/978-3-319-45057-5.